

3 **WMSAN Python Package: From Oceanic Forcing to
4 Synthetic Cross-correlations of Microseismic Noise.**

5 **Lisa Tomasetto**  * ¹, **Pierre Boué**  ¹, **Fabrice Ardhuin**  ², **Éléonore Stutzmann**  ³, **Zongbo Xu**  ³, **Raphaël De Plaen**  ⁴, **Laurent Stehly**  ¹

7 ¹Institut des Sciences de la Terre, CNRS, IRD, Université Gustave Eiffel, Université Grenoble Alpes, University of Savoie Mont Blanc,
8 Grenoble, France, ²Laboratoire d'Océanographie Physique et Spatiale (LOPS), Univ. Brest, CNRS, IRD, Ifremer, IUEM, Brest, France,
9 ³Université Paris Cité, Institut de physique du globe de Paris, CNRS, Paris, France, ⁴Seismology–Gravimetry, Royal Observatory of
10 Belgium, Brussels, Belgium

11 Author contributions: *Conceptualization*: Lisa Tomasetto, Pierre Boué. *Methodology*: Lisa Tomasetto, Pierre Boué, Laurent Stehly, Éléonore Stutzmann,
12 Fabrice Ardhuin,. *Software*: Lisa Tomasetto. *Validation*: Éléonore Stutzmann, Zongbo Xu, Fabrice Ardhuin, Raphaël De Plaen. *Formal Analysis*: Lisa
13 Tomasetto. *Investigation*: Lisa Tomasetto. *Resources*: Pierre Boué. *Writing - Original draft*: Tomasetto Lisa. *Writing - Review & Editing*: Lisa Tomasetto,
14 Pierre Boué, Éléonore Stutzmann, Zongbo Xu, Fabrice Ardhuin, Laurent Stehly, Raphaël De Plaen. *Visualization*: Lisa Tomasetto. *Supervision*: Pierre Boué,
15 Laurent Stehly. *Project administration*: Pierre Boué. *Funding acquisition*: Pierre Boué.

16 **Abstract** Seismic ambient noise spectra show ubiquitously two amplitude peaks correspond-
17 ing to distinct oceanic wave interaction mechanisms called primary ($T \approx 14\text{s}$) and secondary (T
18 $\approx 7\text{s}$) microseismic peaks. Seismic noise records are used in a wide range of applications includ-
19 ing crustal monitoring, imaging of the Earth's deep interior using noise correlations, and studies
20 on the coupling between oceans and solid Earth. All of these applications could benefit from a ro-
21 bust knowledge of spatiotemporal dynamics of microseismic sources. Consequently, seismologists
22 have been studying how to model microseismic sources of ambient noise with the recent improve-
23 ments in ocean wave models. Global sea state and its derivative products are now covering the past
24 decades in models such as the WAVEWATCHIII hindcast. This paper introduces Wave Model Sources
25 of Ambient Noise (WMSAN, pronounced [wam-san]) Python package. This modular package uses
26 standardized wave model outputs to visualize ambient noise source maps and efficiently compute
27 synthetics of seismic spectrograms and cross-correlations for surface waves (Rayleigh) and body
28 waves (P, SV), in a user-friendly way.

29 **Non-technical summary** Continuous oscillations of the ground recorded everywhere on
30 Earth, called seismic ambient noise, show significant peaks in amplitude around 7s and 14s. These
31 correspond to seismic waves originating from interactions between oceanic waves with themselves
32 or with the sea floor at the coast respectively. Seismic ambient noise studies focus on retriev-
33 ing information on the Earth's structure at different scales and depths. Knowing seismic waves'

*Corresponding author: lisa.tomasetto@univ-grenoble-alpes.fr

source spatiotemporal evolution is crucial to extracting the physical characteristics of the sampled medium. Recent developments in oceanic wave modeling from oceanography, through satellite and buoy data assimilation, have opened new opportunities for seismologists to understand recorded seismic waveforms. In this study, we introduce Wave Model Sources of Ambient Noise (WMSAN, pronounced [wam-san]) Python package to visualize ambient noise sources maps and compute proxy of seismic observables in an efficient user-friendly fashion.

1 Introduction

Ocean waves and extreme climate conditions have been known to generate oscillations of the Earth recorded continuously on seismographs since early prototypes by [Bertelli \(1872\)](#). These ubiquitous signals have been of great interest amongst seismologists in the last decades with the development of seismic interferometry, where cross-correlations of seismic signals are used for imaging and monitoring (e.g., [Sabra et al., 2005](#); [Bensen et al., 2007](#); [Lin et al., 2008](#); [Haned et al., 2016](#)). Assuming implicitly a favorable distribution of noise sources, noise correlations in the secondary microseism band but not only, have been used in a wide range of applications such as imaging the Earth at different scales (e.g., [Lu et al., 2018](#); [Boué et al., 2013](#)), monitoring the evolution of the crust (e.g., [Brenguier et al., 2008](#)), and even studying past climate (e.g., [Aster et al., 2023](#)). However, noise sources' dynamic breaks such assumptions and thus may bias measurements, in particular, some early studies have shown that global microseismic sources follow a seasonal pattern that impacts cross-correlations (e.g., [Stehly et al., 2006](#); [Fichtner, 2014](#); [Valero Cano et al., 2024](#)).

Ocean waves generate energetic signals in three distinct period bands of the noise spectrum, namely the hum with periods larger than 30s, the primary microseisms surging around the 14-30s period band, and the secondary microseisms emitting across 3-14s of period (e.g., [Hasselmann, 1963](#); [Ardhuin et al., 2015, 2019](#)).

The hum was the least understood phenomenon, and there have been several hypotheses involving both primary and secondary microseism generation (e.g., [Fukao et al., 2010](#); [Nishida, 2013, 2014](#)). Nevertheless, hum generated from interactions of infragravity waves with a sloping bottom at continental shelves is the most quantitatively valid when comparing modeled and data time series (e.g., [Ardhuin et al., 2015, 2019](#)). On the contrary, primary and secondary microseisms have been extensively studied since the mid-twentieth century to explain seismological observations inland, (e.g., [Longuet-Higgins, 1950](#); [Hasselmann, 1963](#)). The primary microseism mechanism ensues from the interaction of an oceanic wave train and a topographic bottom close to the coast, which results in a seismic wave with a similar frequency to the ocean wave (e.g., [Darbyshire and Okeke, 1969](#); [Ardhuin, 2018](#)). The secondary microseism mechanism, which is the most energetic in amplitude, results from a non-linear interaction between wave trains traveling in opposite directions with similar oscillating periods, the resulting seismic waves present a dominant frequency at twice the oceanic wave frequencies (e.g., [Longuet-Higgins, 1950](#); [Hasselmann, 1963](#); [Kibblewhite and Ewans, 1985](#)). Secondary microseismic sources are distributed globally, also punctual direct observations of both surface and body waves from these sources were reported for extreme cyclones (e.g., [Oliver, 1962](#); [Vinnik, 1973](#)). More recently, back-projection methods or match field processing have allowed better images of source distributions in secondary microseisms period band (e.g., [Neale et al., 2017](#); [Meschede et al., 2019](#); [Retailleau and Gaultier,](#)

69 2019; Igel et al., 2023). Still, having a resolved knowledge of secondary microseismic noise source distribution from
70 seismic data remains an issue with seismic stations mostly located on continents. Comparison between noise dis-
71 tribution from seismic data and spatially well-resolved numerical oceanic wave models shows satisfying similarities
72 (e.g., Arduin et al., 2011; Stutzmann et al., 2012; Nishida and Takagi, 2022; Zhang et al., 2023), also long-time seismic
73 data analysis could give feedback information to improve these models.

74 The WAVEWATCHIII (WW3DG, 2019) oceanographic hindcast model sub-product, computed by IFREMER (Ard-
75 huin et al., 2011), allows comparison with a default 3 hours resolution to seismic data. Its accuracy has been eval-
76 uated in several studies and seismic application fields (e.g., Arduin et al., 2011; Stutzmann et al., 2012; Gaultier
77 et al., 2014; Farra et al., 2016; Tomasetto et al., 2024). However, using these models to compute seismic proxies, such
78 as spectrograms (see the Appendix) or cross-correlations, requires geophysics and ocean sciences knowledge. We
79 present WMSAN for Wave Model Sources of Ambient Noise, a user-friendly Python package to help seismologists
80 model their observations through maps of ambient noise sources from WW3 outputs, but also to compute spectro-
81 grams (e.g., Arduin et al., 2011; Stutzmann et al., 2012; Lecocq et al., 2020) and seismic noise correlations (Ermert
82 et al., 2020).

83 Significant wave height, defined as the mean wave height of the third of the highest waves, should not be used as
84 a proxy for seismic noise amplitude because the exact source mechanism has to be taken into account. We intend
85 to physically describe seismic noise generation, considering bathymetry and wave-induced pressure in the water
86 column. This package aims to be a useful tool for data analysis in ambient noise studies and to pave the way for
87 further cooperation between seismology and oceanography. WMSAN will stay an open and collaborative package
88 that aims to connect with other codes such as noisi (Ermert et al., 2020). For now, this package focuses exclusively
89 on the secondary microseismic peak, however, other forcing, such as hum and primary microseisms, could also be
90 implemented.

91 This report will first describe the main theory underpinning the WW3 products and how it can be used to build
92 secondary microseism source maps, synthetic spectrograms, and synthetic cross-correlations. Then, detailed exam-
93 ples describe this package's applications. Each example described here can be found as the default Jupyter Notebooks
94 tutorial, a summary of currently available examples can be found in the Appendix Table 1. Details on the software
95 accessibility, performance, and documentation can be found in the Data and Code Availability section, and the Ap-
96 pendix.

97 2 Theory: Secondary Microseisms Modeling

98 This section explains the modeling of secondary microseismic sources for P, SV, and Rayleigh waves from WW3 out-
99 puts and amplification coefficients at the source location, considering a 2-layers medium ocean crust and ignoring
100 the sedimentary layer. Secondary microseisms, or double frequency microseisms, result from the non-linear inter-
101 action of ocean gravity wave trains of similar frequencies $f_1 \approx f_2$ traveling in opposite directions. This interaction
102 induces pressure changes close to the ocean surface, which generates seismic waves propagating within the Earth.
103 Three configurations can lead to such a mechanism, described in Arduin et al. (2011). First, within a given storm, a
104 steady wind generates waves in all directions which interact among them. Second, oceanic waves travel to the coast,

105 are reflected, and interact with the incoming waves. Third, two ocean waves generated from different storms can
 106 propagate over long distances before interacting. The WW3 hindcast model provided by IFREMER ([WW3DG, 2019](#))
 107 provides the pressure sources from 1993 to 2022. The model includes pressure sources resulting from the interac-
 108 tion of ocean wave coastal reflection with incoming waves, used for seismology applications [Ardhuin et al. \(2011\)](#).
 109 We then compute the effect of bathymetry to obtain seismic source terms for the given seismic wave type.

110 2.1 Spectral Density of the Wave Induced Pressure

111 We follow the notation from [Farra et al. \(2016\)](#) in this section. The secondary microseismic source computation first
 112 depends on the directional wave spectrum $F(r, f, \theta) = E(r, f)M(r, f, \theta)$, where the power spectrum of the vertical
 113 sea surface displacement $E(r, f)$ is punctually given by buoy and satellite data, and $M(r, f, \theta)$ gives the directional
 114 distribution of elevation for each frequency. Then the spectral density of the wave-induced pressure just below the
 115 sea surface F_p , in $\text{Pa}^2 \cdot \text{m}^2 \cdot \text{s}$ is computed as:

$$116 F_p(r, 2f) = [2\pi]^2 [\rho_w g]^2 2f E^2(r, f) \int_0^\pi M(r, f, \theta) M(r, f, \theta + \pi) d\theta \quad (1)$$

117 where, r is the coordinate vector, ρ_w is the water's density, g the standard acceleration of gravity, f the oceanic
 118 wave frequency and θ the ocean gravity wave direction angle. F_p is directly given as a WW3 output ([WW3DG, 2019](#)),
 119 therefore WMSAN depends on the availability of these files (from 1993 to 2022 presently). We provide a Python library
 120 that reads and transforms F_p into products easily useable by seismologists. Now that the wave-induced pressure is
 121 known, we focus on energy transmission to the crust by computing bathymetry effects for a given seismic wave type.

122 2.2 Site Effects or Amplification Coefficients

123 Site effects, or amplification coefficients, act as a spatial amplitude modulator in the source computation. The ocean
 124 acoustic wave generated by secondary microseismic sources transmission to the crust might differ depending on the
 125 seismic frequency and incident angle. [Kedar et al. \(2008\)](#); [Ardhuin et al. \(2011\)](#); [Stutzmann et al. \(2012\)](#); [Gaultieri et al.](#)
 126 ([2013, 2014](#)) extensively described how site effects can be computed for Rayleigh waves using surface waves modal
 127 decomposition and body waves using plane wave approximation. In the following paragraphs, we recall how these
 128 coefficients are calculated following [Gaultieri et al. \(2014\)](#) and [Longuet-Higgins \(1950\)](#) for body and Rayleigh waves,
 129 respectively. Let us note that we only focus on vertical motion transmission to the seafloor, so SH and Love waves
 130 are not taken into account here but have been observed and discussed in previous studies (e.g. [Nishida and Takagi,](#)
 131 [2016; Juretzek and Hadzioannou, 2016; Ziane and Hadzioannou, 2019; Gaultieri et al., 2020, 2021](#)).

132 Secondary microseismic ambient noise records are dominated by surface waves which are therefore widely used
 133 (e.g., [Sabra et al., 2005](#); [Bensen et al., 2008](#); [Lu et al., 2018](#)), so modeling Rayleigh waves generation has been an exten-
 134 sive field ([Kedar et al., 2008](#); [Ardhuin et al., 2011](#); [Stutzmann et al., 2012](#); [Gaultieri et al., 2014](#); [Gimbert and Tsai, 2015](#)).
 135 As in [Gaultieri et al. \(2013\)](#) a surface waves modal representation of the elastic displacement field is widespread in
 136 the literature, in particular, the fundamental mode for Rayleigh waves predominates the signal. We follow [Longuet-](#)
 137 [Higgins \(1950\)](#) tables to compute the amplitude response functions of the Rayleigh waves modal decomposition, for

138 a pressure field at the ocean surface over a crustal half space as:

$$139 \quad C(f_s, h) = \sum_{i=1}^4 c_i(f_s, h)^2 \quad (2)$$

140 where h is the water column depth and $f_s = 2f$ the seismic frequency, and f the ocean frequency. This simple
141 approach could be improved in future package versions, recomputing the c_i coefficients with different medium ve-
142 locities and densities, for higher modes, but also include sedimentary layers effects as in [Gimbert and Tsai \(2015\)](#).

143 For body waves, assuming a plane wave traveling in the water layer and transmitted to the crust, therefore ne-
144 glecting the sediment layer, the amplification coefficient for body waves is as follows:

$$145 \quad c_{P/SV}(f_s, h) = \sqrt{\int_0^{\theta_{P_w}^*} \left| \frac{T_{P/SV}(\theta_{P_w})}{1 + R(\theta_{P_w} \exp^{i\phi_w(h(r), 2\pi f_s, \theta_{P_w})})} \right|^2 d\theta_{P_w}} \quad (3)$$

146 where, h the ocean depth, θ_{P_w} (default critical angle 15.71°) the P/SV-wave takeoff angle range, ϕ_w the plane P/SV-
147 wave potential propagating in water, R the seabed interface reflection coefficient and $T_{P/SV}$ the seabed interface
148 P or SV wave transmission coefficient. The body wave amplification depends on the body wave incident angle θ_{P_w}
149 ([Farra et al., 2016](#)). Here we consider a proxy of this amplification by integrating over all angles which enables to
150 have a single coefficient for each source location. The takeoff angles higher than 15.71° are not accounted for since R
151 and $T_{P/SV}$ coefficients become complex, and we are not interested in evanescent waves ([Gualtieri et al., 2014](#)). The
152 sediment layer is negligible if its thickness is lower than half the wavelength of the studied seismic waves, which is
153 the case in most oceans in the 3-10s period band, $\leq 6\text{km}$ ([Straume et al., 2019](#)).

154 Once the spectral density of the wave-induced pressure in the ocean layer and the site effect at the seafloor in-
155 terface are defined, we introduce default examples to visualize and compare ambient noise sources computed in a
156 wave model (WW3) to real data.

157 3 WMSAN to Compute Sources, Synthetic Cross-Correlations and Spectrograms, 158 Based on Ocean Wave Models

159 The WW3 wave model is a state-of-the-art community-driven ocean wave hindcast, constrained by buoy and satellite
160 data, integrating wave height, water depth, and surface current data. Useful outputs to seismologists are the spectral
161 density of the induced wave pressure (p2l) and bathymetry files, saved in NetCDF format. Each of these products
162 can be found on the Ifremer ftp <ftp://ftp.ifremer.fr/ifremer/ww3/HINDCAST/SISMO/> (e.g., [Ardhuin et al., 2011](#)). The grid
163 used by default in the package has a 0.5° resolution in both latitude (ranging from 78°S to 80°N) and longitude (from
164 180°W to 179.5°E). It spans 22 frequencies from 0.08 to 0.61 Hz with a 3-hour time step from 1993 to 2022. This package
165 only provides tools to compute seismic data proxy. We don't provide tools to handle recorded seismic data, since
166 other Python packages can be used to calculate data counterparts (e.g., [Lecocq et al., 2014](#); [Krischer et al., 2015](#); [Jiang](#)
167 and [Denolle, 2020](#)). Alternatively, one may recompute the wave-induced pressure from the full directional spectra
168 archived by the European Center for Medium-range Weather Forecasting; either in their operational analysis and
169 forecasts or in reanalyses such as ERA5 (e.g., [Hersbach et al., 2020](#)). The ECMWF wave spectra do not include coastal
170 reflections and use slightly different parameterization, resulting in different spectral shapes and wave-induced pres-

sure levels.

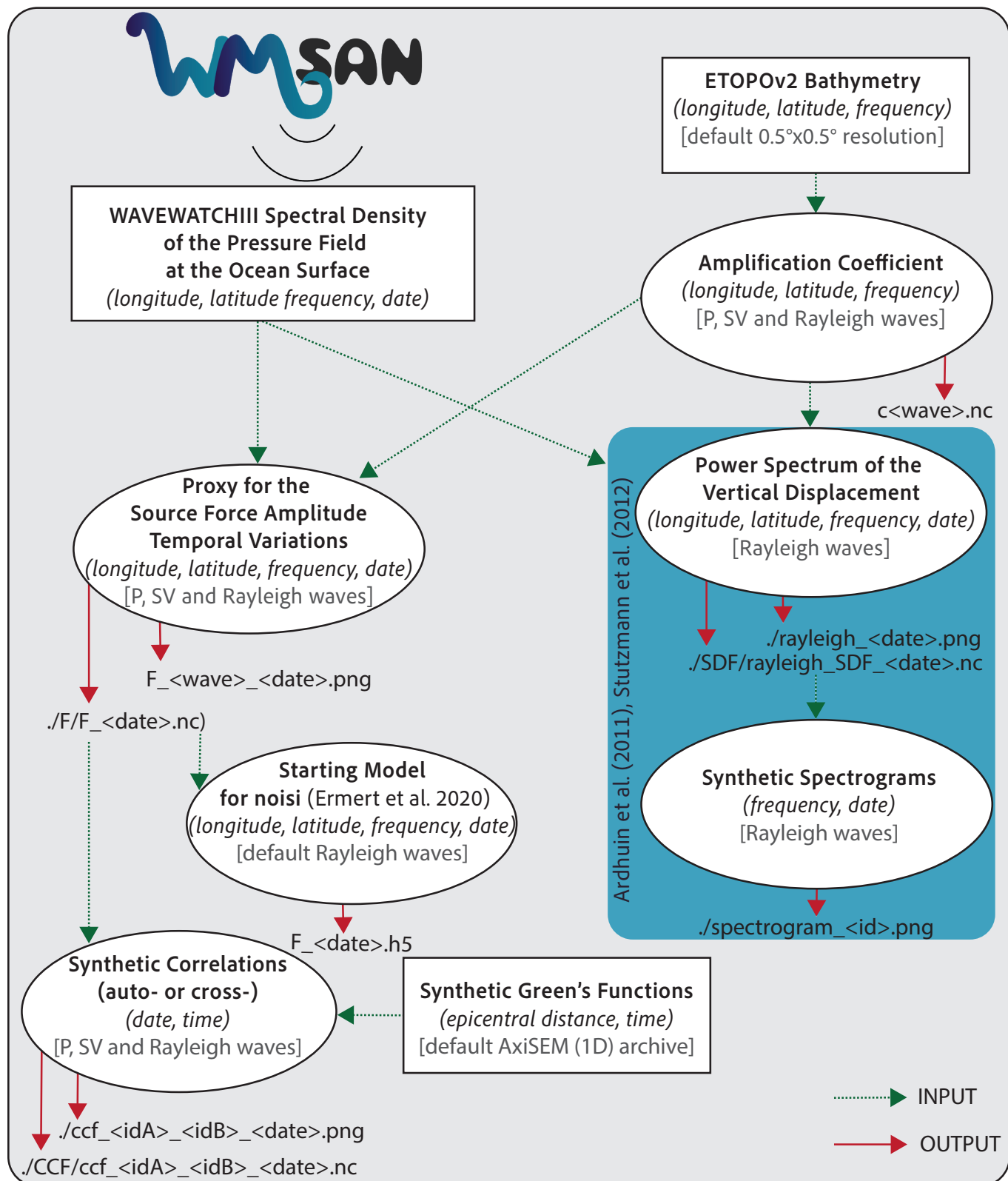


Figure 1 Diagram representation of the different products available in WMSAN and their interactions. Green dotted line represent the input dataset to provide to the package functions, some are given by default. Red plain arrows represent each function's default output file names and format.

171

172 Figure 1 diagram describes the different package's outputs and how they connect. Six different outputs are available
 173 in this package, the site effect computation on refined grids; surface wave synthetic spectrograms as computed
 174 in Ardhuin et al. (2011) and Stutzmann et al. (2012); source maps including amplification coefficients effect; temporal

variations for the source in a given area and synthetic auto- and cross-correlations. Square boxes represent external entities used as inputs, we denote the WW3 spectral density of the pressure field (F_p) and the bathymetry used to compute the previously described site effects. One can either use the default bathymetry or use a thinner grid such as the 1 arc min resolution given by the ETOPO Global Relief Model [NOAA National Centers for Environmental Information \(2022\)](#), specific grids such as the coast of Africa or New Caledonia are also available. Each external element is used to compute the Rayleigh waves synthetic spectrograms (details in the Appendix) and source maps.

3.1 Source Maps: Proxy for the Source Amplitude

Sources are computed on the whole ocean's surface grid provided by WW3 as the amplitude of the vertical force applied on the sea surface modulated by the previously described site effect, as described in previous studies ([Zhang et al., 2023](#); [Boué and Tomasetto, 2024](#); [Tomasetto et al., 2024](#)). This proxy for the source is an estimation of the effective force amplitude, which includes local propagation effects, only a proxy in the case of body waves. Each site effect relies on different assumptions, normal mode summation for Rayleigh waves, and plane wave approximation for body waves. Therefore, this proxy should not be interpreted as the vertical force applying on the seafloor but as an approximation for the source distribution. We define this proxy of the source amplitude as F_{prox} (in N) as:

$$F_{\text{prox}}|_i(r) = 2\pi \sqrt{\int_{f_{s_{\min}}}^{f_{s_{\max}}} (c)^2(r, f_s) F_p|_i(r, f_s, K \approx 0) dA df_s} \quad (4)$$

where i is the date step with a 3-hr resolution, r the location on the grid, $dA = R^2 \cos(\lambda) d\lambda d\phi$ the cell's surface element, R the Earth's radius, λ the latitude, and ϕ the longitude. The c symbol denotes the site effect of the wave type of interest, for body waves, we use $c_{P/SV}(f_s, h)$ and $C(f_s, h)$ for Rayleigh waves, as described in equations 2 and 3 respectively. The corresponding Jupyter Notebooks for Rayleigh waves and body waves can be found in [/notebooks/rayleigh_waves/microseismic_sources.ipynb](#) and [/notebooks/body_waves/microseismic_sources.ipynb](#) respectively. The custom site effect can be computed for Rayleigh waves, corresponding to the functions used in the Jupyter Notebook entitled [/notebooks/rayleigh_waves/amplification_coefficients.ipynb](#). Similarly, an estimate of body waves' site effect (P and SV) can be computed for a given bathymetry using the Jupyter Notebook entitled [/notebooks/body_waves/amplification_coefficients.ipynb](#).

Figure 2 shows an example of the resulting maps for each type of seismic wave, the first three Mondays (05, 12, and 19) of January 2014. As pointed out by [Gaultieri et al. \(2014\)](#), P-waves are more amplified than SV-waves, which might explain why the latter is rarely observed in the 3-10s period band ([Nishida and Takagi, 2016](#)). Also, the seasonality of such sources is retrieved, with stronger sources in the Northern Hemisphere from October to March, and stronger sources in the Southern Hemisphere from April to September. Rayleigh waves are enhanced within smaller and sharper-edged areas than their body wave counterparts. The Rayleigh wave amplitude appears between P and SV wave levels. These maps can be used either as is, to visualize the spatiotemporal distribution of secondary microseisms, or be compared to back-projection (e.g., [Retailleau and Gaultieri, 2021](#)) and source inversion results ([Ermert et al., 2020](#); [Igel et al., 2021, 2023](#)). The package allows saving these maps as matrices, with both spatial and frequency dimensions, to be used as an input to build synthetic cross-correlations (see Figure 1).

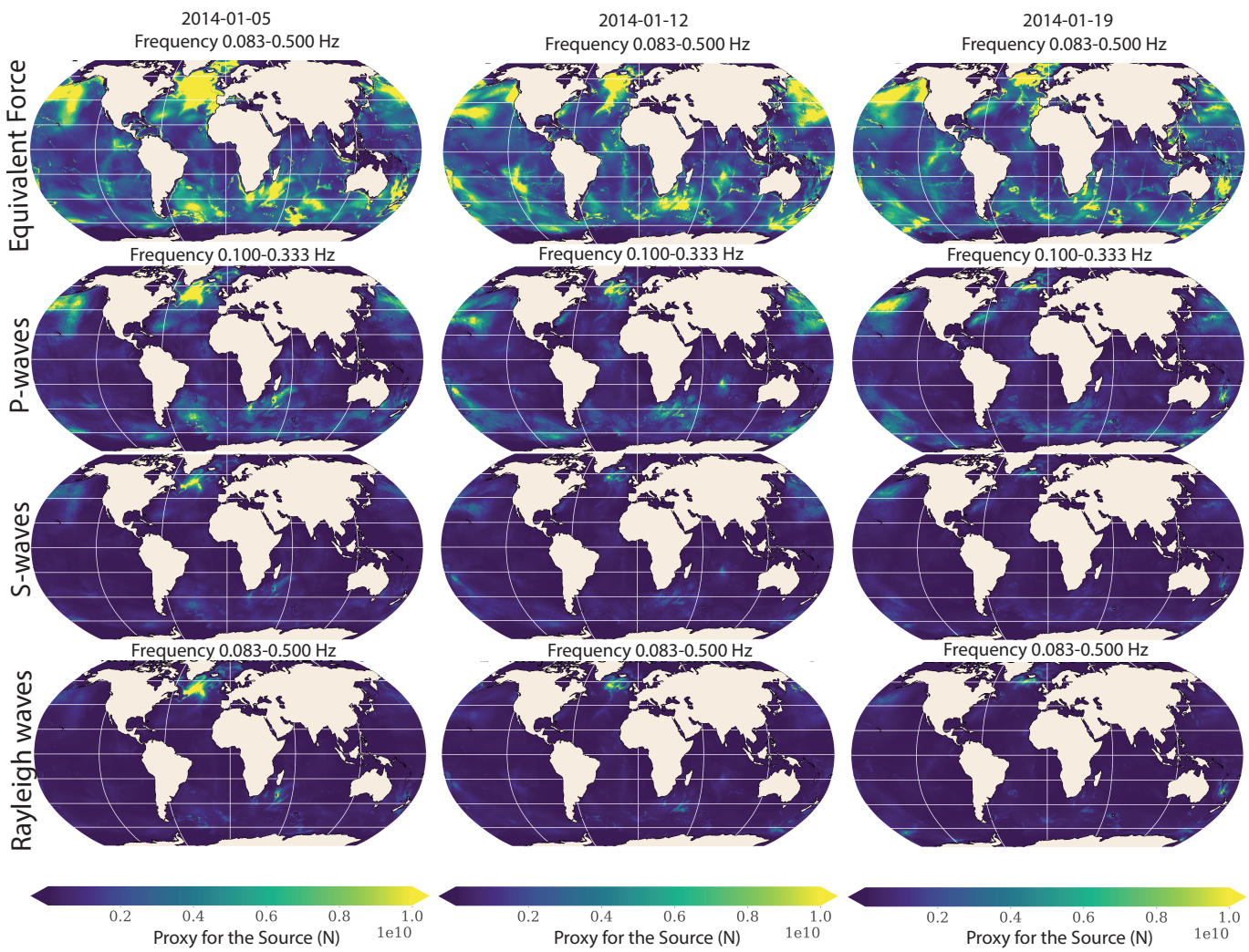


Figure 2 The standard output of WMSAN compared to the equivalent force (top row) without site effect modulation. The proxy for the source amplitude (F) the first three Mondays of January 2014, for P-waves (second row), SV-waves (third row), and Rayleigh-waves (bottom row).

209 3.2 Synthetic Cross-Correlations Implementation

210 The seismic interferometry founding principle relies on the correlation operator between two seismic recordings
 211 to extract or enhance coherency hidden in continuous oscillations. Seismic noise records have been used for many
 212 applications, including monitoring the spatio-temporal evolution of the crust and the subsurface, and seismic imaging
 213 at different scales. This has opened the possibility to supplement the information provided by earthquakes,
 214 (e.g., [Shapiro et al., 2005](#)). Two different interpretations of cross-correlations can be distinguished. The first, more
 215 widespread, assumes that noise correlations provide the Green's function between two sensors, but depends on
 216 strong assumptions such as wavefield equipartition or homogeneous distribution of noise sources (e.g., [Weaver and](#)
 217 [Lobkis, 2002](#); [Sanchez-Sesma and Campillo, 2006](#); [Wapenaar and Fokkema, 2006](#)). The second one considers cross-
 218 correlation without assuming that it corresponds to Green's function of the medium, as a differential measure of wave
 219 propagation (e.g., [Sager et al., 2021](#)). The latter do not rely on strong assumptions but require estimating the source
 220 spatio-temporal evolution to deduce information on the sampled medium. The WMSAN package aims to provide a
 221 convenient way to model oceanic noise sources and compute synthetic correlations. Figure 3 shows the data flow to
 222 compute synthetics cross-correlation between vertical components, as in [Ermert et al. \(2020\)](#) and [Tomasetto et al.](#)

223 (2024). Using the representation theorem and assuming temporally uncorrelated source points (e.g., Wapenaar and
 224 Fokkema, 2006), one can write the cross-correlation function between sensors A and B as:

$$225 \quad C(r_A, r_B, t) = \mathcal{FT}^{-1} \left[\int_{\partial D} G(r_A, r, f_s) G^*(r_B, r, f_s) S(r, f_s) dr \right] \quad (5)$$

226 with $G(r_A, r, f_s)$ the Green's function between a source in r and station A in r_A . The star symbol * denotes the complex
 227 conjugate and ∂D the spatial domain of potential sources, here the ocean's surface. The inverse Fourier transform is
 228 written as \mathcal{FT}^{-1} . The source term $S(r, f_s) = 4\pi^2 C^2(r, f_s) F_p|_i(r, f_s, K \approx 0) dA$ represents a proxy of the source's PSD
 229 at position r , given by the square of proxy for the source amplitude for Rayleigh waves. Therefore, we do not expect to
 230 retrieve the amplitude of the real data cross-correlation, but a first estimate of the variability of the cross-correlation
 231 as a function of source distribution and frequency content. The assumption of temporally uncorrelated sources re-
 232 lies on the fact that the source grid has a 0.5° step in both latitude and longitude, so the sea state variations between
 233 two adjacent grid points appear uncorrelated. Also in the case of temporally correlated sources, cross-correlations
 234 show repeating patterns and spurious arrivals, which doesn't seem observed in most examples in the secondary mi-
 235 croseismic band. Here, Green's functions are computed in an axisymmetric laterally invariant Earth model using
 236 AxiSEM (Nissen-Meyer et al., 2014), which do not include the ocean fluid layer. Since we intend specifically to model
 237 Rayleigh waves, we window surface waves and discard other arrivals. This prevents the contribution of cross-term.
 238 Also, we do not observe other significant interferences in the example below, which can be explained by incoher-
 239 ent noise in the records or instrumental threshold for detection. Also, the Green's Functions used are computed
 240 with laterally averaged attenuation and dispersion, therefore we illustrate a simple case in the following section by
 241 only focusing on a homogeneous area for wave propagation. The corresponding Jupyter Notebook can be found in
 242 [/notebooks/rayleigh_waves/synthetic_CCF.ipynb](#). This package only provides the possibility to compute synthetic
 243 cross-correlations in a 1D model, to compute more realistic cross-correlations in 3D models we suggest the user run
 244 noisi ([Ermert et al., 2020](#)). A function to link both packages is available to use the WMSAN output as a starting model
 245 for noisi as shown in Figure 3. WMSAN provides a function to taper specific phases in the Green's function archive,
 246 which is not the case in noisi, therefore our package might be useful to focus on specific body wave phase interfer-
 247 ences (PP-P, see [/notebooks/body_waves/synthetic_CCF.ipynb](#)).

248 3.3 Example for a Single Station Pair

249 Next, we show that the transit of a storm for a few days generates Rayleigh waves and how wave models can help us
 250 understand waveform variations in cross-correlation functions.

251 We focus on 6 days from 14 to 20 November 2014, during which a strong source occurred in Northern Iceland
 252 in the North Atlantic that we selected from [Nishida and Takagi \(2022\)](#) catalogs. We pick two seismic stations from
 253 the LAPNET network in northern Finland ([Kozlovskaya, 2007](#)), XK.LP51.00 and XK.SGF.00 which path is oriented to-
 254 wards the source area. The LAPNET network has been used in previous studies to detect P-waves from secondary
 255 microseismic sources ([Poli et al., 2012a; Boué et al., 2013](#)) and is located on the Northern Baltic shield known to have
 256 a quite homogeneous crust ([Poli et al., 2012b](#)), leading to the relevant use of laterally uniform Earth models Green's
 257 functions (ak135f). The package is built to be adjustable, so one could also use Green's Functions computed in a dif-

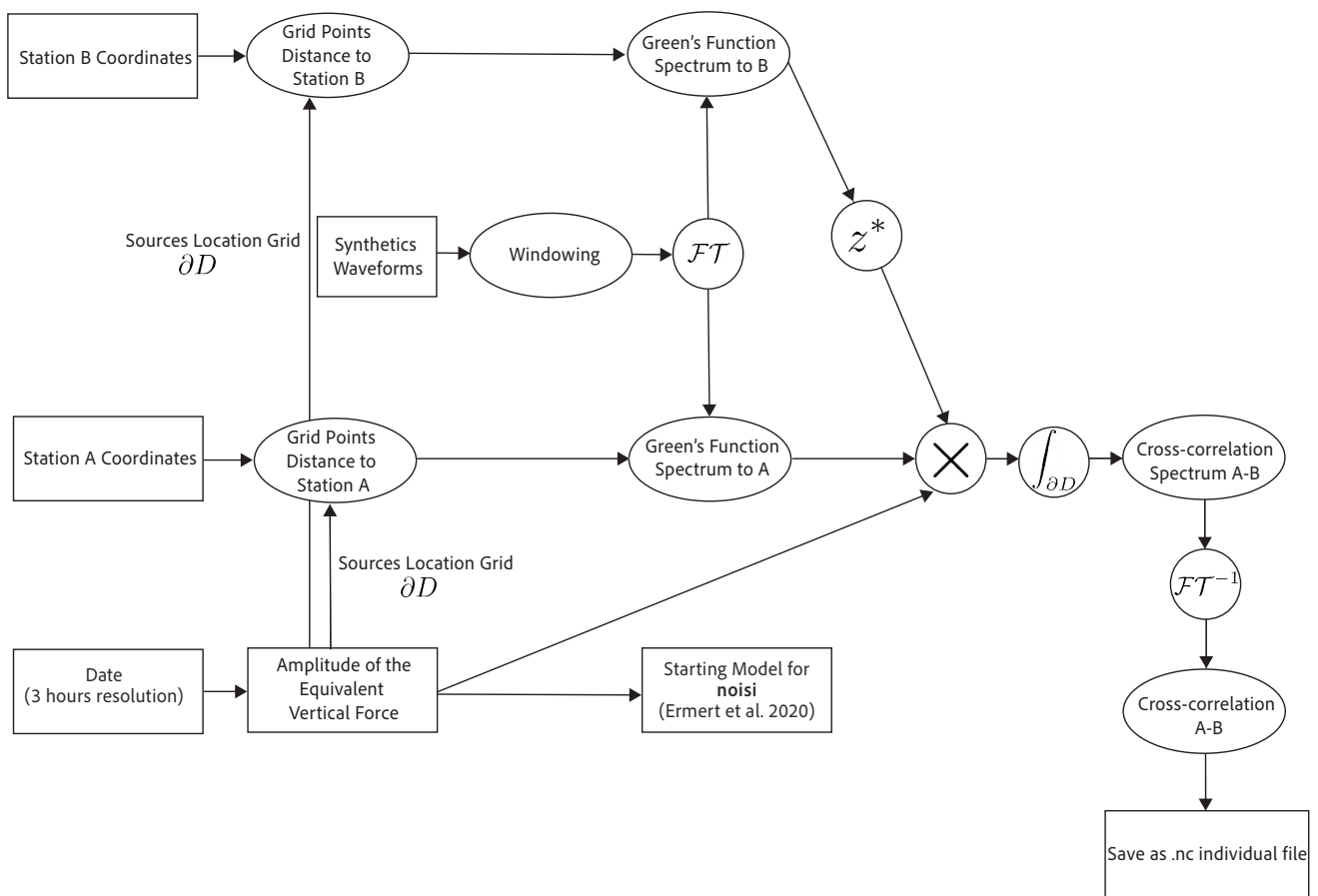


Figure 3 Data flow representing synthetics computation script. Based on representation theorem formulation (Aki and Richards, 2002; Nakata et al., 2019).

258 ferent model as input, for example, computed with AxiSEM (Nissen-Meyer et al., 2014). Other synthetic seismogram
 259 software, such as instaseis (van Driel et al., 2015), are not yet implemented with the package but can be used via noisi
 260 (Ermert et al., 2020). Figure 4a) shows the proxy for the source force amplitude, including Rayleigh waves site effect,
 261 summed over 14-20 November 2008 computed as previously described and the two stations' locations. Equation 5
 262 depends on the source PSD and Green's Functions between each potential source point, imposed by the wave model
 263 grid. We use AxiSEM precomputed Green's Functions in ak135f model with PREM attenuation (Kennett et al., 1995;
 264 Dziewonski and Anderson, 1981), sampled at 1Hz propagating for 3600s for a vertical point force of 10^{20} N, shown in
 265 Figure 4b). Figure 4b) shows the distance-time Green's functions waveforms used, which has a 0.1° distance sampling.
 266 The red and green lines depict velocities of 4.2 km/s and 2.5 km/s respectively, used for the Green's Function tapering.

267 Synthetic cross-correlations with site effect modulation (left) are computed every 3 hours and compared to their
 268 data counterpart (right) in Figure 4c). The figure shows cross-correlations' causal and acausal parts normalized by the
 269 maximum value over the whole panel to highlight the amplitude variations. No particular post-processing has been
 270 done to remove earthquakes, we present raw cross-correlations. The maximum amplitudes appear from the 18th of
 271 November at noon to the 19th at noon with site effect modulation, matching the data amplitude variations. Rayleigh
 272 waves' arrival times correspond for both synthetic and data, around 35s on the causal part (from KP51 to SGF), which
 273 is explained by the homogeneous medium sampled, the East European Craton. Synthetic cross-correlation without
 274 site effect can be computed, it shows less amplitude contrasts than its site effect modulated counterpart, but its
 275 maximum amplitude around midnight on the 18th of November differs from data.

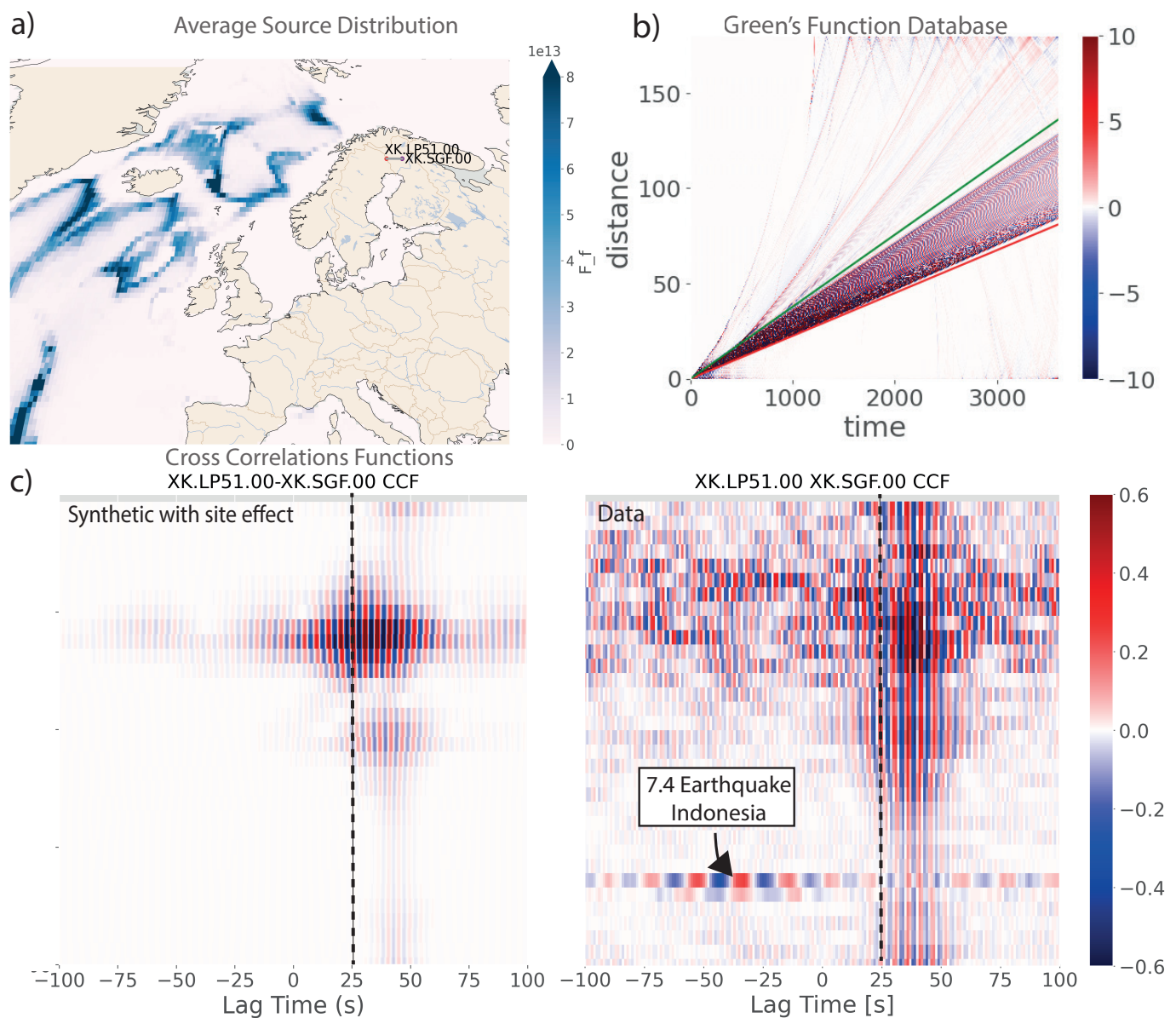


Figure 4 a) Station pair (XK.LP51-XK.SGF) used from the LAPNET network (XK) (Kozlovskaia, 2007) and the source distribution from 14-20 November 2008. b) Synthetic Green's Functions used in the cross-correlation modeling. c) Cross-correlations functions from 16-20 November 2008 split into 3 hr windows. Waveforms normalized by the maximum value of the panel. (left) Synthetic cross-correlation functions with site effect modulation, (right) Data-based cross-correlation functions.

276 Some notable discrepancies between waveforms remain, such as the variations in amplitude on the 16th of
 277 November related to the source modeling, or the main pulse's frequency content. The data is filtered in the 2-10
 278 s period band, similar to the discrete frequency range of the WW3 model (from 0.08 Hz to 0.61 Hz). Recent devel-
 279 opments in wave modeling parameters by Alday and Arduin (2023) using confirmation from infrasound data can
 280 improve the accuracy for frequencies above 0.4Hz. Figure 4c) shows the spatiotemporal evolution of the retrieved
 281 surface wave with variations of tens of seconds in a few hours, so this tool can help discriminate source from propa-
 282 gation contributions and therefore deduce structural effects. One can also discriminate other sources, for example,
 283 a long-period signal is seen in the data on the 16th of November 2008 in the 3-6 p.m. segment, corresponding to a Mw
 284 7.3 teleseismic earthquake in Minnassa Peninsula, Indonesia. Given these points, the medium information present
 285 in the data should be the main origin of waveform mismatch. One can imagine improving the modeling using a
 286 well-resolved 3D model of the studied area.

Finally, this simple modeling can help understand the source spatiotemporal impact on cross-correlations, consequently partly removing uncertainties on the cross-correlations features.

4 Conclusion

We presented the WMSAN Python package, a user-friendly Python library to compute proxy for ambient noise source maps, synthetic spectrograms (see the Appendix), and simple synthetic correlation functions to compare to data counterparts. We hope this tool can help improve collaboration between seismologists and oceanographers, and incite the use of WW3 spectral density of the pressure field at the sea surface instead of significant wave height in seismology studies. To help the user get started with the package, we provide an ensemble of Jupyter Notebooks, detailing the previously described examples. A list of the available notebooks is given in the Appendix, as well as links to the library's documentation. If this tool doesn't bring any significantly new methodological development, it surely answers a need in the community. We also believe oceanographers and climate scientists can use these tools to extract information on past oceanic events from seismic data. We support any comments or contributions to improve future versions of this open-source package.

Acknowledgements

This research was funded by the French National Research Agency (ANR) under the project TERRACORR (ANR-20-CE49-0003).

The authors would like to thank Mickael Accensi who produced the WW3 outputs and teaches how to run WAVEWATCHIII every year in a summer school in Brest, France. We are grateful for the help Laura Ermert provided to link noisi to WMSAN. We also would like to thank all the people who gave feedback during the development of this package: Lalit Arya, Reza D. D. Esfahani, Rémy Monville, Clément Robert, Adrien Soudais, and Yixiao Sheng.

We also thank all technical staff and institutions for allowing seismic and oceanic data to be distributed globally.

Data and Code Availability

Full documentation for the WMSAN library as well as the examples used in this paper are available on a dedicated page: <https://tomasetl.gricad-pages.univ-grenoble-alpes.fr/ww3-source-maps/>. This code is available on the Université Grenoble Alpes' GitLab repository: <https://gricad-gitlab.univ-grenoble-alpes.fr/tomasetl/ww3-source-maps>. It is also mirrored on Lisa Tomasetto's personal GitHub repository. Hosting on Zenodo is available, as well as theETOPO bathymetry file and AxiSEM waveforms database in a separate repository <https://zenodo.org/records/11126562>. The Python library is also distributed on PyPI. It is an open-source library, any contribution or suggestion is welcome.

Competing Interests

The authors have no known competing interests.

317 **Appendix**

318 **Rayleigh Waves Spectrograms**

319 We compute spectrograms using equations given by [Ardhuin et al. 2011](#). [Stutzmann et al. 2012](#) highlighted that an
 320 additional parameter $P(f_s)$ representing the three-dimensional (3D) propagation effects might be needed to model
 321 spectrograms for stations located on islands or near the poles, where ice layers induced variations are poorly mod-
 322 eled. We added this parameter as an option, however, a package based on [Stutzmann et al. 2012](#) will be published
 323 later by the original authors where they adjust the ocean wave coastal reflection and attenuation factor for each sta-
 324 tion. The GitLab repository of the WMSAN project will redirect to the second code as soon as it is available, and we
 325 invite any user to compare and test both packages. [Lecocq et al. 2020](#) used similar analog spectrograms' computation
 using WW3 hindcast to validate extreme floods events in Belgium. We first compute the equivalent source of the

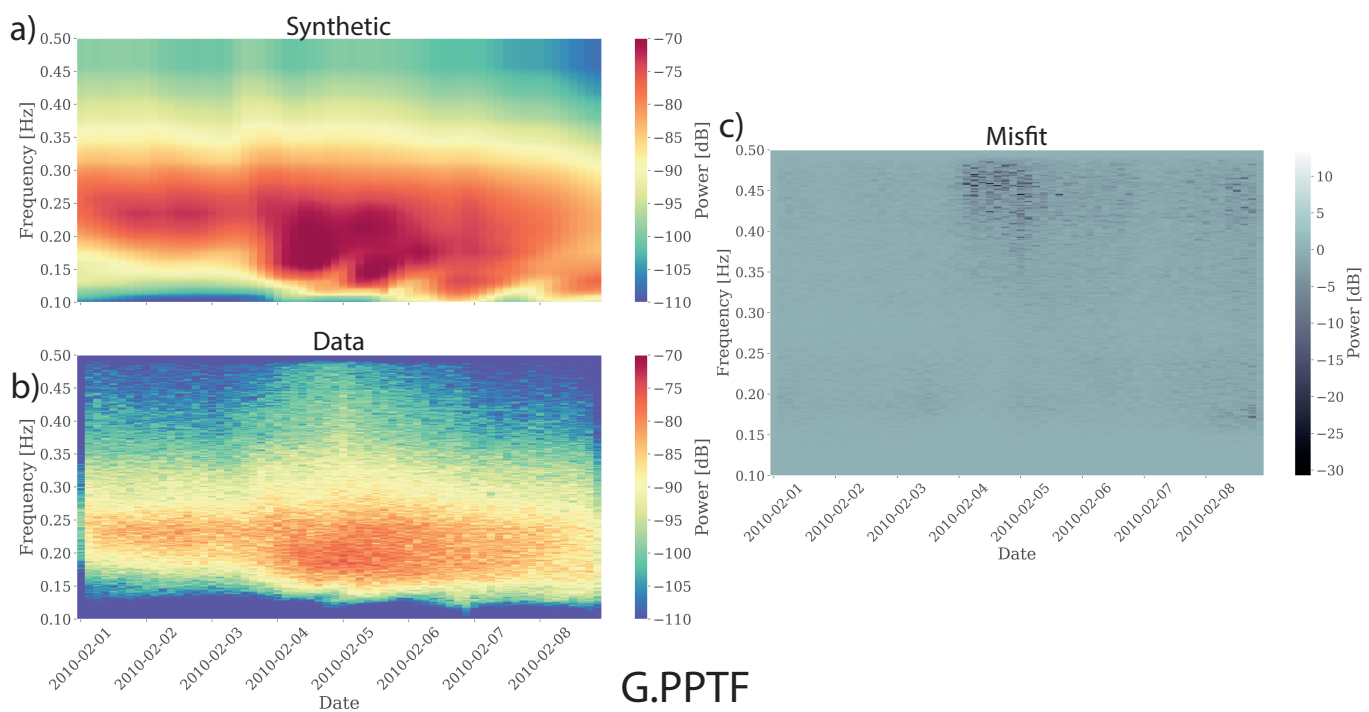


Figure A a) Interpolated synthetic spectrograms with propagation effect coefficient $P(f_s) = 1.9$, and b) data-based spectrograms of stations G.PPTF 1-9 February 2010. c) Misfit between synthetic and data spectrograms as defined in [Stutzmann et al. \(2012\)](#).

326
 327 power spectrum of the vertical displacement $SDF(f_s)$ in m.s, corresponding to the Jupyter Notebook [/notebook-](#)
 328 [s/rayleigh_waves/rayleigh_source.ipynb](#), and defined as:

329

$$S_{DF}(f_s) \approx \frac{2\pi f_s C}{\rho_s^2 \beta^5} F_p(f_s)$$

330 With f_s the seismic frequency in Hz, C the amplitude response functions for the normal modes previously described
 331 (site effect), ρ_s the rock density, and β the shear wave velocity. We then calculate the power spectrum of the vertical
 332 ground displacement at a station of latitude λ and longitude ϕ in $\text{m}^2.\text{s}^{-1}$:

333

$$F_\delta(\lambda, \phi, f_s) = \int_{-\pi/2}^{\pi/2} \int_0^{2\pi} \frac{S_{DF}(f_s)}{R_E \sin \Delta} P(f_s) e^{-2\pi f_s \Delta R_E / (UQ)} R_E^2 \cos \lambda' d\lambda' d\phi'$$

334 with Q the dissipation quality factor, $P(f_s)$ the 3D propagation effect coefficient, Δ the distance between source
 335 and station in radians, R_E the Earth's Radius in meters and U the group velocity of Rayleigh waves in m.s^{-1} . The
 336 corresponding Jupyter Notebook being

337 **/notebooks/rayleigh_waves/spectrograms.ipynb.** We plot the modeled spectrogram at each time step of the model
 338 (default 3-hour resolution) as:

$$339 S_{\text{spectrogram}}(f_s) = 10 \log_{10}(\sqrt{F_\delta(\lambda, \phi, f_s)})$$

340 An example of synthetic spectrograms is shown in Figure A (a) compared to the equivalent data spectrogram (b) fil-
 341 tered between 0.1 Hz and 0.5 Hz for PPTF station from the GEOSCOPE network from 1-9 February 2010([GEOSCOPE](#),
 342 [French Global Network of broad band seismic stations, 1982](#)). We took the values given in [Stutzmann et al. \(2012\)](#)
 343 for the different parameters, such that $Q = 450$, $P = 1.9$, $U = 1800 \text{ m.s}^{-1}$, $\rho_s = 2600 \text{ kg.m}^{-3}$ and $\beta = 2800 \text{ m.s}^{-1}$.
 344 The synthetic spectrogram seems to overestimate amplitudes compared to real data, this might be due to the three-
 345 dimensional wave propagation that is poorly constrained here (constant attenuation factor with distance). Note that
 346 the wave model used for this simulation may differ from the older wave model restricted to 0.1-0.3 Hz used by [Stutz-](#)
 347 [mann et al. \(2012\)](#). We introduce a misfit measure from [Stutzmann et al. \(2012\)](#) that allows the user to compare
 348 synthetic and data quantitatively, as shown in Figure A c). In the PPTF example, the discrepancies in amplitude are
 349 visible in the 0.4-0.5 Hz band, as well as punctual bursts at low frequencies.

350 Corresponding Jupyter Notebooks

| Object to Compute | Jupyter Notebook Path |
|--|---|
| Amplification Coefficient (body waves) | /notebooks/body_waves/amplification_coefficients.ipynb |
| Amplification Coefficient (Rayleigh waves) | /notebooks/rayleigh_waves/amplification_coefficients.ipynb |
| Proxy for the Source Force Amplitude (body waves) | /notebooks/body_waves/microseismic_sources.ipynb |
| Proxy for the Source Force Amplitude (Rayleigh waves) | /notebooks/rayleigh_waves/microseismic_sources.ipynb |
| Spectrograms (Rayleigh waves) | 1) /notebooks/rayleigh_waves/rayleigh_sources.ipynb 2) /notebooks/rayleigh_waves/spectrogram.ipynb |
| Synthetic Cross-correlations (Rayleigh waves) | 1) /notebooks/rayleigh_waves/microseismic_sources.ipynb 2) /notebooks/rayleigh_waves/synthetic_CCF.ipynb or 2) /notebooks/rayleigh_waves/wmsan_to_noisi.ipynb |

Table 1 Table summing up the directory where each example of WMSAN can be found and in what order.

351 Table 1 summarizes the possible values to compute and which Jupyter Notebooks to run to reproduce the figures
 352 shown in this article. Numbers indicate in which order to run Notebooks for the synthetic spectrograms and cross-
 353 correlation functions cases.

354 Python Functions Performance

355 Table 2 gives the run time of the main functions in each Jupyter Notebook, illustrating the formerly detailed examples.

| Object | Notebook | Function | Runtime |
|--|---------------------------------|--|--|
| Download WW3 Files | Several | subfunctions_rayleigh_waves.download_ww3_local | 15 min per monthly file |
| Site effect (body waves) (Rayleigh waves) | amplification_coefficient.ipynb | subfunctions_body_waves.ampli | 10^{-3} s per gridpoint |
| | amplification_coefficient.ipynb | subfunctions_rayleigh_waves.site_effect | 10^{-5} s per gridpoint |
| Force Maps | microseismic_sources.ipynb | subfunctions_rayleigh_waves.loop_WW3 | 10 s per day |
| Temporal Variations | temporal_variations.ipynb | temporal_variation.temporal_evolution | 14 s per month |
| SDF Spectrogram | rayleigh_source.ipynb | subfunctions_rayleigh_waves.loop_SDF | 44 s per day |
| Synthetic Correlations Rayleigh and Body waves Auto-correlation | synthetic_CCF.ipynb | synthetics.compute_ccf | 4.10^{-3} s per grid cell per timestep |
| | synthetic_CCF_autocorr.ipynb | synthetics.compute_ccf_autocorr | 5.10^{-3} s per grid cell per timestep |

Table 2 Performances in terms of run time of the main functions in each Jupyter Notebooks provided as examples.

357 References

- 358 Aki, K. and Richards, P. G. *Quantitative seismology*. 2002.
- 359 Alday, M. and Arduin, F. On Consistent Parameterizations for Both Dominant Wind-Waves and Spectral Tail Directionality. *Journal of*
 360 *Geophysical Research: Oceans*, 128(4):e2022JC019581, 2023.
- 361 Arduin, F. Large-scale forces under surface gravity waves at a wavy bottom: A mechanism for the generation of primary microseisms.
 362 *Geophysical Research Letters*, 45(16):8173–8181, 2018.
- 363 Arduin, F., Stutzmann, E., Schimmel, M., and Mangeney, A. Ocean wave sources of seismic noise. *Journal of Geophysical Research*, 116
 364 (C9):C09004, Sept. 2011. doi: 10.1029/2011JC006952.
- 365 Arduin, F., Gualtieri, L., and Stutzmann, E. How ocean waves rock the Earth: Two mechanisms explain microseisms with periods 3 to 300
 366 s. *Geophysical Research Letters*, 42(3):765–772, Feb. 2015. doi: 10.1002/2014GL062782.
- 367 Arduin, F., Stopa, J. E., Chapron, B., Collard, F., Husson, R., Jensen, R. E., Johannessen, J., Mouche, A., Passaro, M., Quartly, G. D., et al.
 368 Observing sea states. *Frontiers in Marine Science*, 6:124, 2019.
- 369 Aster, R. C., Ringler, A. T., Anthony, R. E., and Lee, T. A. Increasing ocean wave energy observed in Earth's seismic wavefield since the late
 370 20th century. *Nature Communications*, 14(1):6984, Nov. 2023. doi: 10.1038/s41467-023-42673-w.
- 371 Bensen, G., Ritzwoller, M., Barmin, M., Levshin, A. L., Lin, F., Moschetti, M., Shapiro, N., and Yang, Y. Processing seismic ambient noise data
 372 to obtain reliable broad-band surface wave dispersion measurements. *Geophysical journal international*, 169(3):1239–1260, 2007.
- 373 Bensen, G., Ritzwoller, M., and Shapiro, N. M. Broadband ambient noise surface wave tomography across the United States. *Journal of*
 374 *Geophysical Research: Solid Earth*, 113(B5), 2008.
- 375 Bertelli, T. *Osservazioni sui piccoli movimenti dei pendoli in relazione ad alcuni fenomeni meteorologici del p.d. Timoteo Bertelli barnabita*.
 376 Tip. delle scienze matematiche e fisiche, 1872.
- 377 Boué, P. and Tomasetto, L. Opportune detections of global P-wave propagation from microseisms interferometry. *Comptes Rendus. Géosciences*, 356(S4):1–16, 2024.

- 379 Boué, P., Poli, P., Campillo, M., Pedersen, H., Briand, X., and Roux, P. Teleseismic correlations of ambient seismic noise for deep global
380 imaging of the Earth. *Geophysical Journal International*, 194(2):844–848, Aug. 2013. doi: 10.1093/gji/ggt160.
- 381 Brenguier, F., Shapiro, N. M., Campillo, M., Ferrazzini, V., Duputel, Z., Coutant, O., and Nercessian, A. Towards forecasting volcanic eruptions
382 using seismic noise. *Nature Geoscience*, 1(2):126–130, 2008.
- 383 Derbyshire, J. and Okeke, E. A study of primary and secondary microseisms recorded in Anglesey. *Geophysical Journal International*, 17(1):
384 63–92, 1969.
- 385 Dziewonski, A. M. and Anderson, D. L. Preliminary reference Earth model. *Physics of the earth and planetary interiors*, 25(4):297–356, 1981.
- 386 Ermert, L., Igel, J., Sager, K., Stutzmann, E., Nissen-Meyer, T., and Fichtner, A. Introducing noisi: a Python tool for ambient noise cross-
387 correlation modeling and noise source inversion. *Solid Earth*, 11(4):1597–1615, Aug. 2020. doi: 10.5194/se-11-1597-2020.
- 388 Farra, V., Stutzmann, E., Schimmel, M., Gualtieri, L., and Arduin, F. Ray-theoretical modeling of secondary microseism P-waves. *Geophys-
389 ical Journal International*, 206:1730–1739, June 2016. doi: doi: 10.1093/gji/ggw242.
- 390 Fichtner, A. Source and processing effects on noise correlations. *Geophysical Journal International*, 197(3):1527–1531, 2014.
- 391 Fukao, Y., Nishida, K., and Kobayashi, N. Seafloor topography, ocean infragravity waves, and background Love and Rayleigh waves. *Journal
392 of Geophysical Research: Solid Earth*, 115(B4), 2010.
- 393 GEOSCOPE, French Global Network of broad band seismic stations. Institut de physique du globe de Paris (IPGP) and École et Observatoire
394 des Sciences de la Terre de Strasbourg (EOST), 1982. <http://geoscope.ipgp.fr/networks/detail/G/>. doi: 10.18715/GEOSCOPE.G.
- 395 Gimbert, F. and Tsai, V. C. Predicting short-period, wind-wave-generated seismic noise in coastal regions. *Earth and Planetary Science
396 Letters*, 426:280–292, 2015.
- 397 Gualtieri, L., Stutzmann, E., Capdeville, Y., Arduin, F., Schimmel, M., Mangeney, A., and Morelli, A. Modelling secondary microseismic noise
398 by normal mode summation. *Geophysical Journal International*, 193(3):1732–1745, June 2013. doi: 10.1093/gji/ggt090.
- 399 Gualtieri, L., Stutzmann, E., Farra, V., Capdeville, Y., Schimmel, M., Arduin, F., and Morelli, A. Modelling the ocean site effect on seismic
400 noise body waves. *Geophysical Journal International*, 197(2):1096–1106, May 2014. doi: 10.1093/gji/ggu042.
- 401 Gualtieri, L., Bachmann, E., Simons, F. J., and Tromp, J. The origin of secondary microseism Love waves. *Proceedings of the National
402 Academy of Sciences*, 117(47):29504–29511, 2020.
- 403 Gualtieri, L., Bachmann, E., Simons, F. J., and Tromp, J. Generation of secondary microseism Love waves: effects of bathymetry, 3-D
404 structure and source seasonality. *Geophysical Journal International*, 226(1):192–219, July 2021. doi: 10.1093/gji/ggab095.
- 405 Haned, A., Stutzmann, E., Schimmel, M., Kiselev, S., Davaille, A., and Yelles-Chaouche, A. Global tomography using seismic hum. *Geophysical
406 Journal International*, 204(2):1222–1236, 2016.
- 407 Hasselmann, K. A statistical analysis of the generation of microseisms. *Reviews of Geophysics*, 1(2):177–210, 1963.
408 doi: 10.1029/RG001i002p00177.
- 409 Hersbach, H., Bell, B., Berrisford, P., Hirahara, S., Horányi, A., Muñoz-Sabater, J., Nicolas, J., Peubey, C., Radu, R., Schepers, D., et al. The
410 ERA5 global reanalysis. *Quarterly Journal of the Royal Meteorological Society*, 146(730):1999–2049, 2020.
- 411 Igel, J. K. H., Ermert, L. A., and Fichtner, A. Rapid finite-frequency microseismic noise source inversion at regional to global scales. *Geo-
412 physical Journal International*, 227(1):169–183, 05 2021. doi: 10.1093/gji/ggab210.
- 413 Igel, J. K. H., Bowden, D. C., and Fichtner, A. SANS: Publicly Available Daily Multi-Scale Seismic Ambient Noise Source Maps. *Journal of
414 Geophysical Research: Solid Earth*, 128(1):e2022JB025114, 2023. doi: 10.1029/2022JB025114.
- 415 Jiang, C. and Denolle, M. A. NoisePy: A New High-Performance Python Tool for Ambient-Noise Seismology. *Seismological Research Letters*,

- 416 91(3):1853–1866, 04 2020. doi: 10.1785/0220190364.
- 417 Juretzek, C. and Hadzioannou, C. Where do ocean microseisms come from? A study of Love-to-Rayleigh wave ratios. *Journal of Geophysical*
418 *Research: Solid Earth*, 121(9):6741–6756, 2016.
- 419 Kedar, S., Longuet-Higgins, M., Webb, F., Graham, N., Clayton, R., and Jones, C. The origin of deep ocean microseisms in the North Atlantic
420 Ocean. *Proceedings of the Royal Society A: Mathematical, Physical and Engineering Sciences*, 464(2091):777–793, 2008.
- 421 Kennett, B. L., Engdahl, E., and Buland, R. Constraints on seismic velocities in the Earth from traveltimes. *Geophysical Journal International*,
422 122(1):108–124, 1995.
- 423 Kibblewhite, A. C. and Ewans, K. C. Wave–wave interactions, microseisms, and infrasonic ambient noise in the ocean. *The Journal of the*
424 *Acoustical Society of America*, 78(3):981–994, 1985.
- 425 Kozlovskaya, E. Seismic network XK:LAPNET/POLENET seismic temporary array (RESIF-SISMOB), 2007. https://seismology.resif.fr/networks/#/XK__2007. doi: 10.15778/RESIF.XK2007.
- 427 Krischer, L., Megies, T., Barsch, R., Beyreuther, M., Lecocq, T., Caudron, C., and Wassermann, J. ObsPy: a bridge for seismology into the
428 scientific Python ecosystem. *Computational Science and Discovery*, 8(1):014003, may 2015. doi: 10.1088/1749-4699/8/1/014003.
- 429 Lecocq, T., Caudron, C., and Brenguier, F. MSNoise, a Python Package for Monitoring Seismic Velocity Changes Using Ambient Seismic
430 Noise. *Seismological Research Letters*, 85(3):715–726, 05 2014. doi: 10.1785/0220130073.
- 431 Lecocq, T., Arduin, F., Collin, F., and Camelbeeck, T. On the extraction of microseismic ground motion from analog seismograms for the
432 validation of ocean-climate models. *Seismological Research Letters*, 91(3):1518–1530, 2020.
- 433 Lin, F.-C., Moschetti, M. P., and Ritzwoller, M. H. Surface wave tomography of the western United States from ambient seismic noise: Rayleigh
434 and Love wave phase velocity maps. *Geophysical Journal International*, 173(1):281–298, 2008.
- 435 Longuet-Higgins, M. S. A theory of the origin of microseisms. *Philosophical Transactions of the Royal Society of London. Series A, Mathematical*
436 *and Physical Sciences*, 243(857):1–35, 1950.
- 437 Lu, Y., Stehly, L., Paul, A., and Group, A. W. High-resolution surface wave tomography of the European crust and uppermost mantle from
438 ambient seismic noise. *Geophysical Journal International*, 214(2):1136–1150, 2018.
- 439 Meschede, M., Stutzmann, E., and Schimmel, M. Blind source separation of temporally independent microseisms. *Geophysical Journal*
440 *International*, 216(2):1260–1275, 2019.
- 441 Nakata, N., Gaultieri, L., and Fichtner, A. *Seismic ambient noise*. Cambridge University Press, 2019.
- 442 Neale, J., Harmon, N., and Srokosz, M. Monitoring remote ocean waves using P-wave microseisms. *Journal of Geophysical Research: Oceans*,
443 122(1):470–483, 2017.
- 444 Nishida, K. Global propagation of body waves revealed by cross-correlation analysis of seismic hum: BODY WAVE PROPAGATION EXTRACTED
445 FROM SEISMIC HUM. *Geophysical Research Letters*, 40(9):1691–1696, May 2013. doi: 10.1002/grl.50269.
- 446 Nishida, K. Source spectra of seismic hum. *Geophysical Journal International*, 199(1):416–429, 2014.
- 447 Nishida, K. and Takagi, R. Teleseismic S wave microseisms. *Science*, 353(6302):919–921, Aug. 2016. doi: 10.1126/science.aaf7573.
- 448 Nishida, K. and Takagi, R. A Global Centroid Single Force Catalog of P-Wave Microseisms. *Journal of Geophysical Research: Solid Earth*, 127
449 (4):e2021JB023484, 2022. doi: 10.1029/2021JB023484.
- 450 Nissen-Meyer, T., van Driel, M., Stähler, S. C., Hosseini, K., Hempel, S., Auer, L., Colombi, A., and Fournier, A. AxiSEM: broadband 3-D seismic
451 wavefields in axisymmetric media. *Solid Earth*, 5(1):425–445, 2014.
- 452 NOAA National Centers for Environmental Information. ETOPO 2022 15 arc-second global relief model, 2022.

- 453 Oliver, J. A worldwide storm of microseisms with periods of about 27 seconds. *Bulletin of the Seismological Society of America*, 52(3):
454 507–517, 1962.
- 455 Poli, P., Campillo, M., Pedersen, H., and Group, L. W. Body-wave imaging of Earth's mantle discontinuities from ambient seismic noise.
456 *Science*, 338(6110):1063–1065, 2012a.
- 457 Poli, P., Pedersen, H. A., Campillo, M., and the POLENET/LAPNET Working Group. Noise directivity and group velocity tomography
458 in a region with small velocity contrasts: the northern Baltic shield. *Geophysical Journal International*, 192(1):413–424, 11 2012b.
459 doi: 10.1093/gji/ggs034.
- 460 Retailleau, L. and Gualtieri, L. Toward High-Resolution Period-Dependent Seismic Monitoring of Tropical Cyclones. *Geophysical Research
Letters*, 46(3):1329–1337, 2019. doi: 10.1029/2018GL080785.
- 462 Retailleau, L. and Gualtieri, L. Multi-phase seismic source imprint of tropical cyclones. *Nature communications*, 12(1):2064, 2021.
- 463 Sabra, K. G., Gerstoft, P., Roux, P., Kuperman, W., and Fehler, M. C. Surface wave tomography from microseisms in Southern California.
464 *Geophysical Research Letters*, 32(14), 2005.
- 465 Sager, K., Tsai, V. C., Sheng, Y., Brenguier, F., Boué, P., Mordret, A., and Igel, H. Modelling P waves in seismic noise correlations: advancing
466 fault monitoring using train traffic sources. *Geophysical Journal International*, 228(3):1556–1567, 09 2021. doi: 10.1093/gji/ggab389.
- 467 Sanchez-Sesma, F. J. and Campillo, M. Retrieval of the Green's Function from Cross Correlation: The Canonical Elastic Problem. *Bulletin of
the Seismological Society of America*, 96(3):1182–1191, 06 2006. doi: 10.1785/0120050181.
- 469 Shapiro, N. M., Campillo, M., Stehly, L., and Ritzwoller, M. H. High-resolution surface-wave tomography from ambient seismic noise. *Science*,
470 307(5715):1615–1618, 2005.
- 471 Stehly, L., Campillo, M., and Shapiro, N. M. A study of the seismic noise from its long-range correlation properties. *Journal of Geophysical
Research: Solid Earth*, 111(B10), 2006. doi: <https://doi.org/10.1029/2005JB004237>.
- 473 Straume, E. O., Gaina, C., Medvedev, S., Hochmuth, K., Gohl, K., Whittaker, J. M., Abdul Fattah, R., Doornenbal, J. C., and Hopper, J. R.
474 GlobSed: Updated total sediment thickness in the world's oceans. *Geochemistry, Geophysics, Geosystems*, 20(4):1756–1772, 2019.
- 475 Stutzmann, E., Ardhuin, F., Schimmel, M., Mangeney, A., and Patau, G. Modelling long-term seismic noise in various environments. *Geo-
physical Journal International*, 191(2):707–722, 11 2012. doi: 10.1111/j.1365-246X.2012.05638.x.
- 477 Tomasetto, L., Boué, P., Stehly, L., Ardhuin, F., and Nataf, H.-C. On the stability of mantle-sensitive P-wave interference during a secondary
478 microseismic event. *Geophysical Research Letters*, 51(8):e2023GL108018, 2024.
- 479 Valero Cano, E., Fichtner, A., Peter, D., and Mai, P. M. The impact of ambient noise sources in subsurface models estimated from noise
480 correlation waveforms. *Geophysical Journal International*, 239(1):85–98, 2024.
- 481 van Driel, M., Krischer, L., Stahler, S. C., Hosseini, K., and Nissen-Meyer, T. Instaseis: instant global seismograms based on a broadband
482 waveform database. *Solid Earth*, 6(2):701–717, 2015. doi: 10.5194/se-6-701-2015.
- 483 Vinnik, L. Sources of microseismic P waves. *Pure and Applied Geophysics*, 103:282–289, 1973.
- 484 Wapenaar, K. and Fokkema, J. Green's function representations for seismic interferometry. *GEOPHYSICS*, 71(4):SI33–SI46, 2006.
485 doi: 10.1190/1.2213955.
- 486 Weaver, R. and Lobkis, O. On the emergence of the Green's function in the correlations of a diffuse field: pulse-echo using thermal phonons.
487 *Ultrasonics*, 40(1-8):435–439, 2002.
- 488 WW3DG. User Manual and System Documentation of WAVEWATCH III version 6.07, The WAVEWATCH III Development Group. *Tech. Note* 326
489 *pp. + Appendices, NOAA/NWS/NCEP/MMAB*, 2019.

- 490 Zhang, R., Boué, P., Campillo, M., and Ma, J. Quantifying P-wave secondary microseisms events: a comparison of observed and modelled
491 backprojection. *Geophysical Journal International*, 234(2):933–947, 2023.
- 492 Ziane, D. and Hadzioannou, C. The contribution of multiple scattering to Love wave generation in the secondary microseism. *Geophysical
493 Journal International*, 217(2):1108–1122, 2019.